Multi-channel Imager Algorithm (MIA): A novel cloud-top phase classification algorithm

Jiaxi Hu,[a] Daniel Rosenfeld,[b] Yannian Zhu,[c,d] Xin Lu,[e] Jacob Carlin[a]

[a] *Cooperative Institute for Mesoscale Meteorological Studies, University of Oklahoma, and NOAA/OAR National Severe Storms Laboratory, Norman, Oklahoma*

[b] *Department of Atmospheric Sciences, The Hebrew University of Jerusalem, Jerusalem, Israel*

[c] *School of Atmospheric Sciences, Nanjing University, 210023 Nanjing, China*

[d] *Joint International Research Laboratory of Atmospheric and Earth System Sciences & Institute for Climate and Global Change Research, Nanjing University, China*

[e] *State Key Laboratory of Information Engineering in Surveying, Mapping, and Remote Sensing, Wuhan University, Wuhan, China*

Corresponding author: Jiaxi Hu, jiaxi.hu@noaa.gov

ABSTRACT

The current Geostationary Operational Environmental Satellites (GOES-16 and 17) cloud-top phase classification algorithm is based primarily on empirical thresholds at multiple wavelengths that have varying absorption capabilities for water and ice. The performance of current GOES-16 cloud-top phase product largely depends on the accuracy of the selection of reflectance ratios. This study aims at presenting a novel cloud-top phase classification algorithm (the Multi-channel Imager Algorithm, MIA) that provides a more judicious selection of relationships between channels using a supervised K-mean clustering method on multi-channel Red-Green-Blue images. The K-mean clustering method works analogously to how human eyes separate different colors in a microphysical color rendering set of satellite images, which differentiates water, ice and unclassified thin clouds. For water phase, cloud-top temperature information is used to further distinguish supercooled water. To evaluate the performance of the MIA, an extensive comparison with Cloud-Aerosol Lidar with Orthogonal Polarization (CALIOP), Moderate Resolution Imaging Spectroradiometer, and current GOES-16 cloud-top phase products is conducted, using CALIOP as the benchmark. Compared to the current GOES-16 cloud-top phase product, MIA demonstrates a substantial improvement in phase classification, where hit rate increases from 69% to 76% over the Continental United States and 58% to 66% over the full disk domain.

1. Introduction

The work of retrieving satellite cloud phase product has been ongoing for decades and is essential for our understanding of the global radiation budget, weather, and hydrological cycles (Liou 1986; Wielicki et al. 1995). In addition, the presence of supercooled water presents an acute threat to aviation safety due to the risk of aircraft icing (Ellrod and Bailey 2007; Smith et al. 2012). As such, real-time knowledge of cloud phase is highly desirable. Owing to the sparseness of available in-situ observations of cloud phase, much attention has been devoted to deriving cloud phase information with large scale coverage from remote sensing observations.

Satellite cloud phase retrieval methods include using active sensors, which emit their own radiation directed at the intended targets. Examples of such sensors include the Cloud-Aerosol Lidar with Orthogonal Polarization (CALIOP) onboard the Cloud-Aerosol Lidar and Infrared Pathfinder Satellite Observations (CALIPSO) satellite, and the cloud-profiling radar onboard CloudSat (Cesana et al. 2016; Choi et al. 2010; Hu et al. 2010; Hu et al. 2009; Kikuchi et al. 2017; Peterson et al. 2020; Tan et al. 2014; Winker et al. 2010; Yuan et al. 2010) . Active satellite sensors are advantageous in that they can provide information about both the cloud-top phase and the vertical phase distribution within clouds up to the signal saturation limit (e.g., in the case of CALIOP, up to optical thicknesses of approximately 5; (Winker et al. 2010)). However, these sensors only have sparse global coverage. Other attempt includes using multiple satellite product corrected cloud-top phase product (Chen and Sun 2019; Noh and Miller 2018) and etc.

Conversely, satellites with passive sensors only measure radiation emitted or reflected by targets. Compared to the aforementioned active sensors, these sensors offer wider data swaths and thus provide better global coverage. Examples of passive sensors onboard satellites include the Geostationary Operational Environmental Satellite 16/17 (Miller et al. 2014), geostationary Himawari-8 Satellite (Takahashi 2012), Second-generation Global Imager (Nakajima et al. 2019), Polarization and Directionality of the Earth's Reflectances (Weidle and Wernli 2008), Moderate Resolution Imaging Spectroradiometer (Marchant et al. 2016; Morrison et al. 2011; Naud et al. 2006), Atmospheric Infrared Sounder (Naud and Kahn 2015), and Advanced Very High Resolution Radiometer (Carro-Calvo et al. 2016). However, since the passive identification of cloud phase depends on emitted or reflected shortwave infrared information, only cloud-top phase can be obtained (Hu et al. 2009).

Geostationary satellites offer the additional benefit of continuous tracking and characterization of cloud systems. Thus, application of a cloud-top phase algorithm to geostationary satellite data permits the evolution of cloud-top phase of individual clouds and cloud systems to be observed in space and time, which is advantageous for both the modeling community and real-time weather forecasters. The current GOES-16 cloud-top phase product (described in further detail in section 2.3) essentially uses reflectance ratios from various near-infrared channels to infer the cloud-top phase. However, the actual values of such ratios can vary between different clouds, illumination levels, and viewing geometries that are not accounted for by the present algorithm. Thus, the algorithm's accuracy is heavily dependent on how thresholds for these ratios are selected.

In this paper, we develop a new cloud-top phase algorithm—the Multi-channel Imager Algorithm (MIA)—for use with geostationary satellite data. The MIA attempts to improve upon the existing GOES-16 classification approach and more flexibly and comprehensively account for these ratios and other factors by applying a supervised machine-learning method that uses multiple GOES-16 satellite channels. Although the algorithm introduced in this paper has only been tested on GOES-16 data, equivalent principles can be easily applied to the GOES-17, Meteosat Third Generation from Europe, and Himawari-8/9 from Japan, which collectively cover most of the globe.

The rest of this paper is organized as follows. Descriptions of the existing cloud-top phase data that the MIA is compared against are presented in section 2, while a full description of the MIA is provided in in section 3. Section 4 presents the results of these comparisons, as well as a discussion about factors that may inhibit the MIA's performance in certain circumstances. This study's findings are summarized and future work is proposed in section 5.

2. Data

2.1. Cloud-Aerosol Lidar with Orthogonal Polarization (CALIOP)

CALIOP is a dual-wavelength (532 nm and 1064 nm) depolarization lidar (Hunt et al. 2009) onboard the CALIPSO satellite. Since absorption by water and ice hydrometeors is minimal at both of these wavelengths, CALIOP determines cloud phase using the depolarization of backscattered light, which can be used as a good proxy for cloud phase classification (Hu et al. 2009). The underlying assumption is that all water particles are spherical, while ice particles are not and subsequently result in some degree of depolarization (Hu et al. 2001). The latest version of the CALIOP cloud phase product inherited the layer-integrated depolarization ratio method from prior versions and added the spatial correlation of layer-integrated attenuated backscatter as a key parameter for differentiating anisotropic ice crystals from water particles, which can account for as much as a 20% improvement of overall ice cloud observation (Hu et al. 2009). Although the latest CALIOP cloud-phase product shows real promise in its ability to separate randomly and horizontally oriented ice crystals over past versions, there is still room for improvement for thin ice clouds with low signal-to-noise ratios and clouds with discontinuous layers (Hu et al. 2009).

In this study, the CALIOP Lidar Level 2 Vertical Feature Mask (VFM) Version 4-20 cloud phase product is used as the benchmark for evaluating the other examined algorithms as well as the proposed MIA. The phase classifications at 333-m, 1-km, and 5-km resolutions are merged to create a composite phase product for evaluation(Winker et al. 2006). The importance of merging the 1-km and 5-km resolution data from CALIOP for phase classification is discussed in Marchant et al. (2016); here, we also incorporate the 333-m-resolution data to retain as much detailed phase information as possible. By default, CALIOP's phase classification algorithm includes a normal ice phase, a horizontally oriented ice phase, and a liquid water phase. In this study, the normal ice phase and horizontally oriented ice phases are combined and treated as a single ice phase to facilitate comparisons with other algorithms with a single ice category.

2.2. Moderate Resolution Imaging Spectroradiometer (MODIS)

The MODIS instruments onboard the polar-orbiting Terra and Aqua satellites have been operating since 1999 and 2002, respectively. MODIS measures reflected and emitted radiation at 36 spectral channels ranging from 405 nm to 14.385 μm with a spatial resolution of 1 km at nadir (Justice et al. 1998).

In this study, we evaluate the daytime portion of the latest MODIS Atmosphere Level-2 Cloud Product (MYD06_L2; Marchant et al. 2016) from Aqua satellite (ascending daytime). This algorithm uses a simple majority vote logic using the (1) 1-km cloud-top temperature, (2) 1-km IR cloud phase, (3) 1.38-μm cirrus detection test for cloud masking, and (4) 1.6-, 2.1-, and 3.7-μm channel derived cloud-top effective radius based on thresholds derived from previous comparisons with CALIOP. The key improvement in the current version is the use of composite look-up tables for ice and water using all three cloud effective radius retrievals, which inherently account for viewing angle geometry and cloud optical thickness. Parameters (1), (2), and (3) otherwise primarily serve as a sanity check. Other differences with respect to the previous version include the use of the IR cloud phase instead of emissivity ratios for parameter (2), the removal of the shortwave IR ratio threshold limit that was affected by instrument differences (Marchant et al. 2016), and an updated decision logic. MYD06_L2 phase product includes clear sky, liquid water, undetermined phase, and ice phase classifications. In this study, only liquid water and ice phases are selected for comparison with CALIOP.

2.3. Geostationary Operational Environmental Satellite 16 (GOES-16)

The instrument of most relevance onboard the GOES-16 satellite is the Advanced Baseline Imager (ABI). The ABI is the primary imaging instrument and includes 16 spectral bands with wavelengths ranging from 0.47 μm to 13.3 μm. The horizontal resolution of bands ranges from 0.5 km to 2 km (Schmit et al. 2017). In this study, all ABI data with finer resolutions are converted to a 2-km resolution for simplicity and consistency. The temporal resolution for GOES-16 data ranges from 60 s (e.g., in the Mesoscale Domain Sector, MDS) to 5 min (e.g., for the Continental United States, CONUS) and 10 min (e.g., for the full disk, FD). Although the high temporal resolution in the MDS would likely permit cloud-top phase classifications even for fast evolving clouds, its odds of being collocated with the CALIOP and MODIS overpasses are scarce. Therefore, the cases selected in this study use only the CONUS and FD resolutions.

The current GOES-16 ABI Cloud-top Phase (ACTP) product uses a two-layer cloud model composed of liquid and ice phases for classifying cloud-top phase (Miller et al. 2014). The accompanying look-up tables are based on Santa Barbara DISORT Atmospheric Radiative Transfer (SBDART) calculations for cloud optical thickness, cloud-top effective radius, and Sun/satellite geometry (Ricchiazzi et al. 1998). The ACTP's assumption for cloud phase detection is that the reflectance ratios (at 1.6 and 2.2 μm) of the ABI input data and an idealized all-liquid cloud behave similarly. The accuracy of the ACTP is strongly related to the assumed reflectance ratio thresholds and is likely subject to failures due to sub-pixel heterogeneity. As an additional input, the ABI clear-sky mask (ACM) level-2 product from GOES-16 is included as a measure to mask non-cloudy pixels (Heidinger and Straka 2012). The ACM provides a binary clear or cloudy mask generated every 5 min for the CONUS and 10 min for the FD at a spatial resolution of 2 km. The ACM thresholds were trained by data from the Spinning Enhanced Visible and InfraRed Imager (SEVIRI) onboard the Meteosat collocated with the CALIPSO retrieval products. A preliminary ACM test shows a 91.4% of correct detection of clear or cloudy state using an 8-week dataset distributed among four seasons (Heidinger and Straka 2012). A detailed overview of ACM performance can be found in Jiménez (2020). The output of the ACTP classification includes clear sky, liquid water, supercooled water, mixed phase, and ice with a 2-km resolution. A detailed description of the ACTP product can be found in Miller et al. (2014). In this study, only liquid water and ice phase are selected in comparison with CALIOP.

3. Algorithm description

A flowchart describing the overall MIA algorithm logic is presented in Figure 1. As mentioned from 2.3, the input data for MIA are Level 1 observations from ABI onboard GEOS-16 at: the visible bands at 0.47 µm, near-infrared bands 1.6 µm, and 2.2 µm are used for the daytime microphysical Red-Green-Blue (DMRGB) color scheme calculation (detailed in section 3.1), while the infrared bands at 11.2 µm and 12.3 µm are used for the cloud-top temperature calculation (detailed in section 3.3).

3.1. Daytime microphysical RGB (DMRGB)

The physical basis for the DMRGB is shown in Figure 2, which shows the imaginary part of the refractive index (a measure of the degree of absorption) for water and ice at different wavelengths. The differences in absorption capabilities between ice and water vary with wavelength. For instance, at a wavelength of 1.6 µm (what we consider the red channel), ice absorption is almost an order of magnitude larger than that of water, while at 2.25 µm (what we consider the green channel) water is more absorptive than ice. The opposite absorption responses of ice and water at these two wavelengths allows us to easily highlight the sharp differences between water and ice in the RGB composite. This approach is unlikely to work as well using MODIS data because the green channel in MODIS is at a wavelength of 2.1 μm (Figure. 2), which exhibits similar absorption differences between water and ice as the 1.6 μm wavelength. Therefore, MODIS does not create a color contrast between water and ice clouds if the DMRGB scheme is applied.

Figure 3a shows an example RGB composite using the DMRGB bands (i.e., 1.6, 2.2, and 0.47 μm reflectance in the red, green and blue beams, respectively). The DMRGB color scheme takes advantage of the different absorption capabilities of ice and water between these three bands to highlight cloud top phase information. This method follows the same principle as the RGB schemes in Lensky and Rosenfeld (2008). In this color scheme, ice appears bluish (region A in Fig. 3a) because of its large reflectance at 0.47 μm for ice crystals and strong absorption at 1.6 μm and 2.25 μm (i.e., the extinction of red and green). Water clouds appear pinkish (region B in Fig. 3a) because of the relatively large reflectance at 0.47 μm for water and its much weaker absorption at 1.6 μm compared with ice crystals (up to an order of magnitude difference as shown in Figure 2). Bare ground (region C in Fig. 3a) appears brown because of land's larger reflectance at 2.2 μm than that at 0.47 μm. Ocean (region D in Fig. 3a) appears black because of the low reflectance of all three beams.

3.2. K-mean clustering

Before using K-mean clustering, DMRGB image needs to be converted to L·a·b color space, where "L" represents luminosity layer and "a" and "b" represent chromaticity layers that fall along the red-green and blue-yellow axes, respectively (Jain 1989). This conversion is derived from the commission on illumination L·a·b color space tri-stimulus values. In this study, we use the "rgb2lab" function in Matlab for the conversion from RGB to L.a.b. This conversion helps to downscale the 3D dimensional RGB to 2D dimensional red-green and blue-yellow table, which is required for K-mean clustering in the next step.

K-mean clustering method is only applied to the "a·b" color space where color information exists; the luminosity layer is not required. The K-mean clustering process is a machine-learning method for separating groups of objects and attributing each object to its closest cluster (Arthur and Vassilvitskii 2007), which in this study works analogously to how human eyes differentiate color groups. The Matlab function “imsegkmeans” is used to perform the K-mean clustering, which segments the input “a.b” color space into three clusters and returns the segmented labels. After an initial trial, the number of clustering attempts is limited to 20 to avoid worst sub-optimal local minima and false classifications, but this parameter is customizable depending on user needs.

Figure 3b shows a density map of the chromatic a·b layers of Figure 3a, where three pronounced clusters are observed. Figure 3c shows the corresponding cluster separation estimated from the K-mean clustering process, resulting in three clusters shown in red, green, and blue for ice clouds, optically unclassified thin clouds, and water clouds, respectively (See 3.1. for RGB color scheme). Cloud free pixels (based on the ACM) are excluded. Figure 3d shows the true color extracted from Figure 3a at each red-green and blue-yellow grid point. The bluish color representing the ice phase primarily resides in the lower-left portion of Figure 3d, while the yellow-purple liquid phase pixels dominate the other half of the same panel. The light-yellow end represents clouds with small droplets, whereas the purple end represents clouds with relatively large droplets.

After K-mean clustering, cloud pixels are segmented into clusters corresponding to cloud-top phase. Ideally, given the unique hazard posed by supercooled water, three separate clusters would represent warm water, supercooled water, and ice. Since DMRGB channel combination is only visibly sensitive to the distinguishing of liquid and ice phases, it is hard to separate warm water from supercooled water without cloud-top temperature information. The final step is to apply cloud-top temperature information to all three clusters. Cloud-top temperature is retrieved using the same principle as described in Rosenfeld and Lensky (1998) using brightness temperature information. For liquid pixels, pixels with cloud-top temperatures over 273.15 K are classified as warm water while pixels colder than 273.15 K are considered supercooled water. The cloud-top phase output is then recorded.

4. Algorithm evaluation

To evaluate the performance of MIA, here we present comparisons of the cloud-top phase MIA output (hereafter CTP_MIA) to the current official GOES-16 cloud-top phase product (hereafter CTP_GOES), along with collocated cloud-top phase retrievals from MODIS (hereafter CTP_MODIS) and CALIOP (hereafter CTP_CALIOP), the latter of which serves as the benchmark for evaluation.

In order to test the robustness of MIA, 28 cases from all 4 seasons in 2019 were selected (Table 1). A case is defined as a single half north-to-south CALIOP track that passes over FD and CONUS domains and contains clouds. In instances where multiple tracks overpass FD and CONUS, the one with the most cloud cover is selected. The criteria for case selection are twofold: (a) there are obvious weather systems along the tracks of CALIOP and MODIS overpasses, and (b) the difference in time between the CALIOP and MODIS overpasses is less than 5 minutes. CALIPSO and MODIS used to be synchronized with a time lag of less than 2 minutes. In 2018, they drifted apart, with only a subset of days now providing a match with a time lag of 5 minutes or less. In order to keep all seasons equally represented, we selected 7 cases from each season and selected a total of 28 cases in 2019 for validation in this study.

MIA product case demonstration as an example. Figure 4 shows an example of the MIA output for 27 October 2019. Figure 4a shows the DMRGB map and Figure 4b shows the corresponding cloud-top phase output from the MIA after the clustering analysis is performed. The dotted lines overlapping from left to right represent CTP_CALIOP, CTP_ MODIS, CTP_GOES, and CTP_MIA, respectively. Figure 4c shows the cloud layer phase from CALIOP for this case. The leftmost dotted lines in Figures 4a and 4b represent the highest altitude cloud phase recorded in Figure 4c (i.e. cloud-top phase). A first look between Figure 4a and 4b indicates a reasonable clustering where bluish cloud pixels in Figure 4a are marked in blue (ice phase) and yellow to purple cloud pixels are marked in either pink or green (liquid phase). For instance, all bluish cloud clusters in Figure 4a are labelled as ice phase in Figure 4b. Moreover, even the isolated convective cells in South America are well captured. More insights are observed over the CONUS, where liquid phase cloud clusters are further separated and classified into supercooled liquid and warm water as shown by letters A and B in Figure 4b. The reason the MIA does not identify all of the pixels CALIOP does is that we are only interested in optically thick clouds. Because the MIA works in a similar fashion to human eyes, if one does not visually observe an optically thin cloud in DMRGB, MIA is unlikely to classify such pixels. Additionally, because CTP_MIA, CTP_CALIOP, CTP_GOES, and CTP_MODIS are retrieved from different satellite platforms, there are slight differences in recorded time between them.

Pixel selection criteria used in this study. In this study, CALIOP is used as a benchmark. Two criteria were set for pixel selection for this comparison: (1) a time difference threshold of 5-minute (can be changed accord to users need) is set to eliminate pixels recorded too far away from CALIOP record time. As MODIS and CALIOP have recording times of each pixel, both can easily apply this time difference criterion. For GOES-16, the average of starting and ending time is recognized as the record time for each GOES-16 ABI file. As long as the GOES-16 record time is within 5 minutes of CALIOP recording time range, the GOES-16 data is used for phase processing and comparison; (2) only pixels classified as cloudy by the GOES-16 cloud mask are used as candidates for phase comparison against CALIOP. This means that if a pixel is classified as cloudy only by CALIOP but not by GOES-16, it will not be considered since there is no phase information from the GOES-16 side. Such a case usually occurs to optically thin clouds as shown in Figure 4c and is not a cloud of interest for MIA.

Validation statistics. Boxplots of HIT_MIA (hit rate of MIA), HIT_GOES (hit rate of GOES), and HIT_MODIS (hit rate of MODIS) across FD (full disk, 10-minute resolution) and CONUS (continental US, 5-minute resolution) are shown in Figure 5a and 5b, respectively. As shown in Figure 5a for FD results, MIA median hit rate is 0.66 and standard deviation (STD) is 0.15, whereas HIT_GOES median is 0.58 (STD = 0.22) and HIT_MODIS median is 0.68 (STD = 0.13). This corresponds to 13.7% median hit rate improvements of MIA with respect to CTP_GOES. Figure 5b shows the same statistics for CONUS, where MIA median hit rate is 0.76 and least STD of 0.11. The CONUS HIT_GOES and HIT_MODIS median values are 0.69 and 0.77 with STD values of 0.17 and 0.13, respectively. These results correspond to a significant improvement for CTP_MIA with respect to CTP_GOES. There is a clear improvement in CTP_MIA skill for the CONUS domain versus the FD, which is likely due in part to the higher temporal resolution of the CONUS data. CTP_MODIS outperforms CTP_MIA by marginal percentages.

Geometry effect on phase classification accuracy. To explore the effect of solar zenith angle (SolZ) and satellite zenith angle (SatZ) on algorithm performance, the hit/miss records of data points from all the selected cases are grouped into 10-degree bins of SolZ and SatZ (Figure 6). It is evident that the accuracy of all three algorithms decreases as SolZ and SatZ increase, which is expected as reflectance data tend to be degraded at higher latitudes and further away from nadir. As shown in Figures 6a and 6b, HIT_MIA generally provides a better median hit rate than HIT_GOES does, except at low values of SatZ and SolZ. A similar story is seen for the FD domain, HIT_MIA generally has better relative accuracy than HIT_GOES. CTP_MIA shows increasing skill relative to CTP_GOES and CTP_MODIS at higher values of SolZ and SatZ in the FD domain (Figure 6c and 6d). HIT_MODIS generally outperforms HIT_MIA along SolZ and SatZ gradient.

Understanding of the discrepancies between MIA and CALIOP. To further analyze the causes of discrepancies between CTP_MIA and CTP_CALIOP, pixels where the two disagreed from all cases are presented in Figure 7. Figure 7a shows that the majority of the disagreements occur when the CTP_CALIOP output is ice and the CTP_MIA output is water. At these pixels, the cloud-top temperature difference (Figure 7b) between CTP_MIA (using GOES-16's cloud-top temperatures) and CTP_CALIOP (using CALIOP's cloud-top temperatures) is positive and ranges from close to 0 K to 112 K, which means most points with disagreement between CTP_CALIOP and CTP_MIA have much colder cloud-top temperatures from CALIOP than MIA. This is direct evidence that CALIOP is sensitive to high and cold transparent cirrus clouds while MIA is not, which is as expected since CTP_CALIOP uses active lidar measurements and is sensitive to optically thin cirrus clouds. The objective of MIA is to classify optically thick clouds, and we believe such discrepancies between CTP_MIA and CTP_CALIOP provide the correct phase for the tops of optically thick clouds. In contrast, the disagreement of pixels where CTP_MIA has ice and CTP_CALIOP has water are relatively rare. The corresponding cloud-top temperature differences for this scenario are shown in Figure 7b. We suspect this is caused by differences in the temporal resolution, which can be as large as 5 minutes in this study. The CALIOP cloud-tops are mostly much colder than the GOES-16 cloud-tops when they disagree with respect to the CTP.

A first look at MIA's performance after deleting multi-layer cloud pixels. Finally, we performed a preliminary test of MIA's performance after reducing the temperature discrepancies shown in Figure 7. As previously mentioned, the primary source of these discrepancies is believed to be multi-layer clouds. Lensky and Rosenfeld (2008) showed that the difference in brightness temperature between 10 µm and 12 µm is a robust indicator of optically thin clouds. Here, brightness temperature difference for cirrus (BTD_Cirrus) is defined as the difference between GOES-16 12.3-µm and 10.4-µm brightness temperatures. In order to tackle this problem, we generated a density map of the relationship between BTD_Cirrus and the cloud-top temperatures difference between CALIPSO and GOES-16 (T_diff). Figure 8a shows that most (around 73%) of these pixels are concentrated where both BTD_Cirrus and T_diff are near zero, representing optically thick clouds without overlying thin layers where the algorithms should in theory agree well. We then selected only the pixels with -10<T_diff<2 and BTD_Cirrus>-2, shown as the red rectangle in Fig. 8a. Figures 8b and 8c show similar boxplot patterns as Figure 5 for the selected pixels. The boxplots from both Figure 8b and 8c show significant CTP_MIA median hit rate (CONUS: 91%; FD: 88%) improvements over CTP_GOES (CONUS: 88%; FD: 70%) for both FD and CONUS. It is worth noting that after applying the T_diff and BTD_Cirrus restrictions, the remaining pixels represent the ideal accuracy of MIA compared to CALIOP. Since CALIOP availability is limited by its spatial coverage and temporal resolution, we cannot rely on active sensors to assist with this kind of correction for operational weather satellites. This comparison serves to explain the causes of phase classification discrepancies when they occur, and to bolster confidence in favor of the MIA determination in such cases.

5. Conclusion

In this study we present a novel Multi-channel Imager Algorithm for classifying the phase of optically thick cloud-tops. This algorithm has the potential to greatly benefit the modeling community by providing not just accurate but also continuous cloud-top phase information. MIA is based on a supervised K-mean clustering method with added cloud-top temperature information, which partitions the cloudy pixels into ice, supercooled water, and warm water phases. The MIA demonstrated substantial improvements compared to the current GOES-16 and MODIS cloud-top phase products using CALIOP phase retrievals as a benchmark. In particular, based on the 28 selected cases in 2019, the median hit rate for CONUS increased from 69% to 76% for GOES-16 when using the current phase product and MIA, respectively (the respective numbers for the FD are 58% to 66%). The performance of all methods degrade with increasing satellite and solar zenith angles. However, MIA shows the least degradation, especially near the high end of the angles.

Most of the remaining pixels where MIA classification did not agree with CALIOP's can be explained by a large discrepancy between cloud-top temperatures from GOES-16 and CALIOP. This temperature discrepancy occurred either due to mismatch of the field of view or due to CALIOP observing optically thin clouds, such as cirrus, above optically thick clouds at lower heights. Such a thin upper cloud layer is practically transparent to GOES-16 satellite, which instead quantifies the properties of the underlying optically thick clouds. While a cause of algorithm discrepancies, these optically thin clouds (with geometric thicknesses less than 150 m) have negligible contributions to surface precipitation, which is dominated by clouds with larger geometrical thicknesses (Fan et al. 2020). When only comparing pixels with temperature agreement within 12 K and eliminating thin cirrus, the median hit rate increased to 88% for the GOES-16 algorithm and 91% for the MIA. The respective numbers for the FD are 70% and 88%. These high accuracies are validated by CALIOP, but the disadvantage is that we cannot rely on CALIOP's assist in operation due to its limited time/space coverage.

Finally, although MIA presents substantial improvements compared to the current GOES-16 phase product, we are planning to further improve the algorithm by using neural networks. The current MIA requires DMRGB generation and training at each snapshot, and is unlikely to meet real-time needs. Our next goal is to use the current MIA output as a training dataset and to introduce all ABI channels to neural network training. That will allow us to generate improved cloud phase classification in real time.

Acknowledgments.

Funding was provided by NOAA/Office of Oceanic and Atmospheric Research under NOAA-University of Oklahoma Cooperative Agreement #NA16OAR4320115, U.S. Department of Commerce, and by the U.S. National Weather Service, Federal Aviation Administration, and Department of Defense program for modernization of NEXRAD radars. Additional funding came from the Department of Energy grant DE-SC0018967.

Special thanks to my wife Lishan (Mia) Li for her dedication in the grammar check process during the review period.

Data Availability Statement.

Data used here are obtained from Comprehensive Large Array-Data Stewardship System of the National Oceanic and Atmospheric Administration and Atmospheric Science Data Center of National Aeronautics and Space Administration.

Appendix A: List of variables and their descriptions

AIRS	Atmospheric Infrared Sounder
BTD_Cirrus	Difference between GOES 12.3 and 10.4 brightness temperatures
CALIOP	Cloud-Aerosol Lidar with Orthogonal Polarization

CONUS	Contiguous United States
CTP_ CALIOP	CALIOP cloud-top phase
CTP_ MIA	MIA cloud-top phase
CTP_GOES	GOES-16 cloud-top phase
CTP_MODIS	MODIS cloud-top phase
DMRGB	Daytime microphysical RGB
FD	Full disk
GOES-16	Geostationary Operational Environmental Satellites 16
Himawari	Geostationary weather satellites operated by the Japan Meteorological Agency
HIT_ CALIOP	CALIOP hit rate
HIT_ MIA	MIA hit rate
HIT_GOES	GOES-16 hit rate
HIT_MODIS	MODIS hit rate
L·a·b	Color space defined by the International Commission on Illumination
LUTs	Lookup tables
MDS	Mesoscale Domain Sector
Meteosat	European meteorological program in Geostationary Orbit
MIA	Multi-channel Imager Algorithm
MODIS	Moderate Resolution Imaging Spectroradiometer
POLDER	Polarization and Directionality of the Earth’s Reflectances

RGB	Red Green Blue
SatZ	Satellite zenith angle
SBDART	Santa Barbara DISORT Atmospheric Radiative Transfer
SEVIRI	Spinning Enhanced Visible and Infrared Imager
SolZ	Solar zenith angle
STD	Standard deviation
T_diff	Cloud-top temperatures
VFM	Vertical Feature Mask

REFERENCES

Arthur, D., and S. Vassilvitskii, 2007: *K-Means++: The Advantages of Careful Seeding.* Vol. 8, 1027-1035 pp.

Carro-Calvo, L., C. Hoose, M. Stengel, and S. Salcedo-Sanz, 2016: Cloud glaciation temperature estimation from passive remote sensing data with evolutionary computing. *Journal of Geophysical Research: Atmospheres*, **121,** 13,591-513,608.

Cesana, G., and Coauthors, 2016: Using in situ airborne measurements to evaluate three cloud phase products derived from CALIPSO. *Journal of Geophysical Research: Atmospheres*, **121,** 5788-5808.

Chen, Z., and X. Sun, 2019: Dynamic spatial fusion of cloud top phase from PARASOL, CALIPSO, cloudsat satellite data. *Journal of Quantitative Spectroscopy and Radiative Transfer*, **224,** 176-184.

Choi, Y.-S., R. S. Lindzen, C.-H. Ho, and J. Kim, 2010: Space observations of cold-cloud phase change. *Proceedings of the National Academy of Sciences*, **107,** 11211.

Ellrod, G. P., and A. A. Bailey, 2007: Assessment of Aircraft Icing Potential and Maximum Icing Altitude from Geostationary Meteorological Satellite Data. *Weather and Forecasting,* **22,** 160-174.

Heidinger, A., and W. C. Straka, 2012: Algorithm Theoretical Basis Document: ABI Cloud Mask.

Hu, Y.-X., D. Winker, P. Yang, B. Baum, L. Poole, and L. Vann, 2001: Identification of cloud phase from PICASSO-CENA lidar depolarization: a multiple scattering sensitivity study. *Journal of Quantitative Spectroscopy and Radiative Transfer*, **70,** 569-579.

Hu, Y., and Coauthors, 2010: Occurrence, liquid water content, and fraction of supercooled water clouds from combined CALIOP/IIR/MODIS measurements. *Journal of Geophysical Research: Atmospheres*, **115**.

Hu, Y., and Coauthors, 2009: CALIPSO/CALIOP Cloud Phase Discrimination Algorithm. *J Atmos Ocean Tech*, **26,** 2293-2309.

Hunt, W. H., D. M. Winker, M. A. Vaughan, K. A. Powell, P. L. Lucker, and C. Weimer, 2009: CALIPSO Lidar Description and Performance Assessment. *J Atmos Ocean Tech*, **26,** 1214-1228.

Jain, A. K., 1989: *Fundamentals of Digital Image Processing.* Prentice Hall.

Jiménez, P. A., 2020: Assessment of the GOES-16 Clear Sky Mask Product over the Contiguous USA Using CALIPSO Retrievals. *Remote Sens-Basel*, **12,** 1630.

Justice, C. O., and Coauthors, 1998: The Moderate Resolution Imaging Spectroradiometer (MODIS): land remote sensing for global change research. *Ieee T Geosci Remote*, **36,** 1228-1249.

Kikuchi, M., and Coauthors, 2017: Development of Algorithm for Discriminating Hydrometeor Particle Types With a Synergistic Use of CloudSat and CALIPSO. *Journal of Geophysical Research: Atmospheres*, **122,** 11,022-011,044.

Lensky, I. M., and D. Rosenfeld, 2008: Clouds-Aerosols-Precipitation Satellite Analysis Tool (CAPSAT). *Atmos Chem Phys*, **8,** 6739-6753.

Liou, K.-N., 1986: Influence of Cirrus Clouds on Weather and Climate Processes: A Global Perspective. *Monthly Weather Review*, **114,** 1167-1199.

Marchant, B., S. Platnick, K. Meyer, G. T. Arnold, and J. Riedi, 2016: MODIS Collection 6 shortwave-derived cloud phase classification algorithm and comparisons with CALIOP. *Atmos Meas Tech*, **9,** 1587-1599.

Miller, S. D., Y.-J. Noh, and A. K. Heidinger, 2014: Liquid-top mixed-phase cloud detection from shortwave-infrared satellite radiometer observations: A physical basis. *Journal of Geophysical Research: Atmospheres*, **119,** 8245-8267.

Morrison, A. E., S. T. Siems, and M. J. Manton, 2011: A Three-Year Climatology of Cloud-Top Phase over the Southern Ocean and North Pacific. *J Climate*, **24,** 2405-2418.

Nakajima, T. Y., and Coauthors, 2019: Theoretical basis of the algorithms and early phase results of the GCOM-C (Shikisai) SGLI cloud products. *Progress in Earth and Planetary Science*, **6,** 52.

Naud, C. M., and B. H. Kahn, 2015: Thermodynamic Phase and Ice Cloud Properties in Northern Hemisphere Winter Extratropical Cyclones Observed by Aqua AIRS. *J Appl Meteorol Clim*, **54,** 2283-2303.

Naud, C. M., A. D. Del Genio, and M. Bauer, 2006: Observational Constraints on the Cloud Thermodynamic Phase in Midlatitude Storms. *J Climate*, **19,** 5273-5288.

Noh, Y.-J., and S. D. Miller, 2018: Chapter 3 - Detection of Mixed-Phase Clouds From Shortwave and Thermal Infrared Satellite Observations. *Mixed-Phase Clouds*, C. Andronache, Ed., Elsevier, 43-67.

Peterson, C. A., Q. Yue, B. H. Kahn, E. Fetzer, and X. Huang, 2020: Evaluation of AIRS Cloud Phase Classification over the Arctic Ocean against Combined CloudSat–CALIPSO Observations. *J Appl Meteorol Clim*, **59,** 1277-1294.

Ricchiazzi, P., S. Yang, C. Gautier, and D. Sowle, 1998: SBDART: A Research and Teaching Software Tool for Plane-Parallel Radiative Transfer in the Earth's Atmosphere. *B Am Meteorol Soc*, **79,** 2101-2114.

Rosenfeld, D., and I. M. Lensky, 1998: Satellite-based insights into precipitation formation processes in continental and maritime convective clouds. *B Am Meteorol Soc*, **79,** 2457-2476.

Schmit, T. J., P. Griffith, M. M. Gunshor, J. M. Daniels, S. J. Goodman, and W. J. Lebair, 2017: A Closer Look at the ABI on the GOES-R Series. *B Am Meteorol Soc*, **98,** 681-698.

Smith, W. L., P. Minnis, C. Fleeger, D. Spangenberg, R. Palikonda, and L. Nguyen, 2012: Determining the Flight Icing Threat to Aircraft with Single-Layer Cloud Parameters Derived from Operational Satellite Data. *J Appl Meteorol Clim*, **51,** 1794-1810.

Takahashi, T., 2012: Precipitation particle charge distribution and evolution of East Asian rainbands. *Atmospheric Research*, **118,** 304-323.

Tan, I., T. Storelvmo, and Y.-S. Choi, 2014: Spaceborne lidar observations of the ice-nucleating potential of dust, polluted dust, and smoke aerosols in mixed-phase clouds. *Journal of Geophysical Research: Atmospheres*, **119,** 6653-6665.

Weidle, F., and H. Wernli, 2008: Comparison of ERA40 cloud top phase with POLDER-1 observations. *Journal of Geophysical Research: Atmospheres*, **113**.

Wielicki, B. A., R. D. Cess, M. D. King, D. A. Randall, and E. F. Harrison, 1995: Mission to Planet Earth: Role of Clouds and Radiation in Climate. *B Am Meteorol Soc*, **76,** 2125-2154.

Winker, D. M., C. Hostetler, M. A. Vaughan, and A. and Omar, 2006: CALIOP algorithm theoretical basis document, part 1: CALIOP instrument, and algorithms overview.

Winker, D. M., and Coauthors, 2010: The CALIPSO Mission: A Global 3D View of Aerosols and Clouds. *B Am Meteorol Soc*, **91,** 1211-1230.

Yuan, T., J. V. Martins, Z. Li, and L. A. Remer, 2010: Estimating glaciation temperature of deep convective clouds with remote sensing data. *Geophys Res Lett*, **37**.

TABLES

Winter	Spring	Summer	Fall
20190108	20190308	20190613	20190917
20190110	20190309	20190614	20190918
20190130	20190328	20190702	20191005
20190217	20190329	20190720	20191007
20190218	20190416	20190721	20191025
20191220	20190506	20190808	20191027
20191221	20190524	20190810	20191114

Table 1. Cases selected for performing the CTP_MIA, CTP_GOES, CTP_MODIS, and CTP_CALIOP comparison.

FIGURES

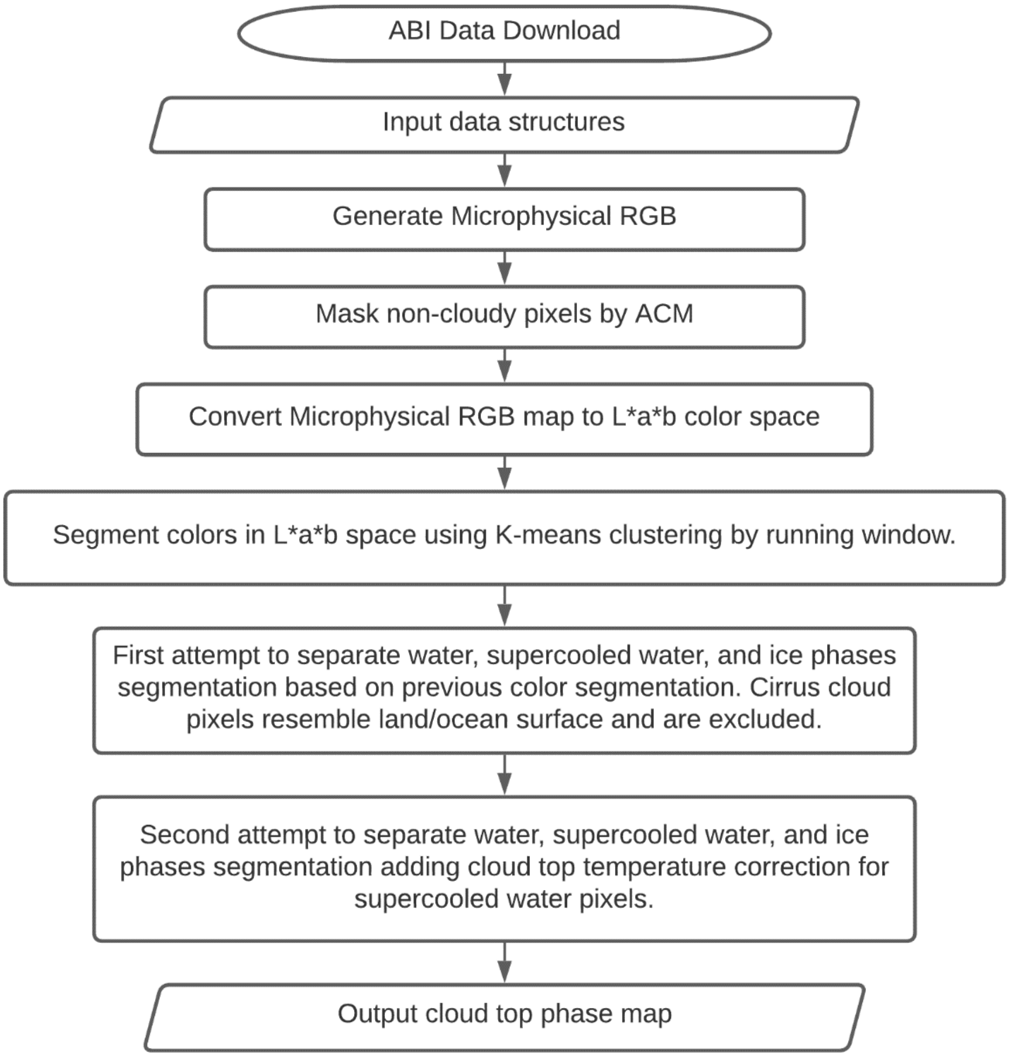

Figure 1. Multi-channel Image Algorithm general logic flowchart.

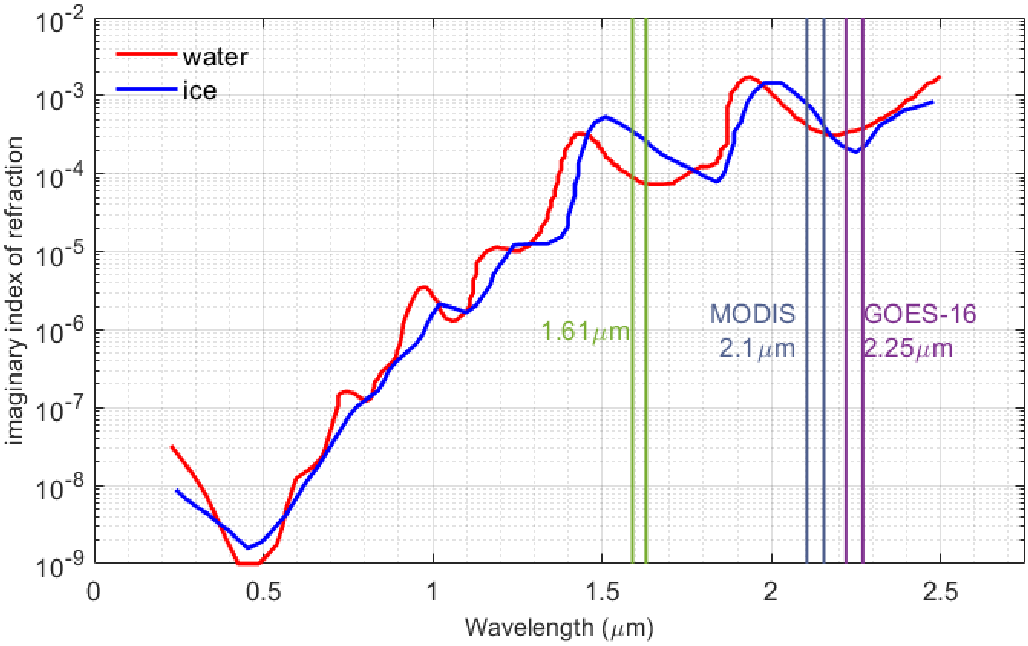

Figure 2. Imaginary part of the refractive index of ice and water as a function of wavelength between 0.25 and 2.5 μm. Each pair of colored vertical lines corresponds to the marked channel wavelength range.

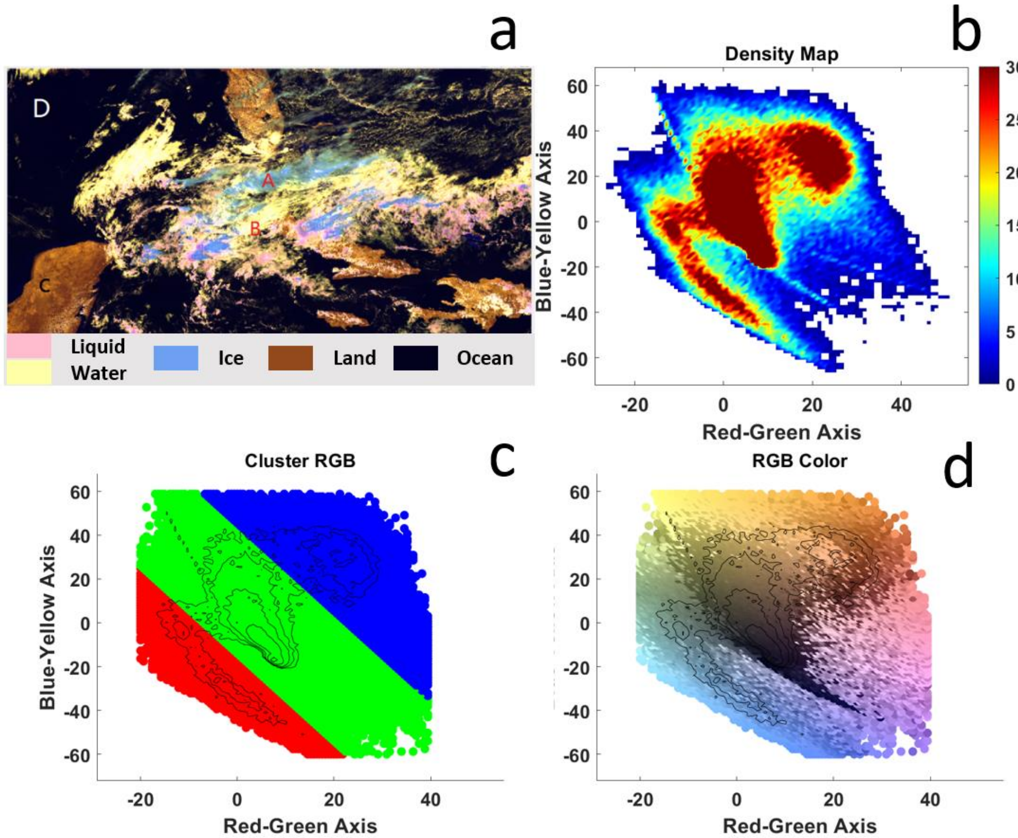

Figure 3. (a) Daytime microphysical RGB map and (b) the corresponding pixel density map of the chromaticity layers along the red-green axis in the abscissa and blue-yellow axis in the ordinate. The K-mean clustering output of (b) is shown in (c) as water phase (blue), unclassified optically thin clouds (green), and ice clouds (red). The real color RGB distribution from (a) along the chromatic layers is shown in (d). The contours in panels (c) and (d) represent the pixel density as shown in (b).

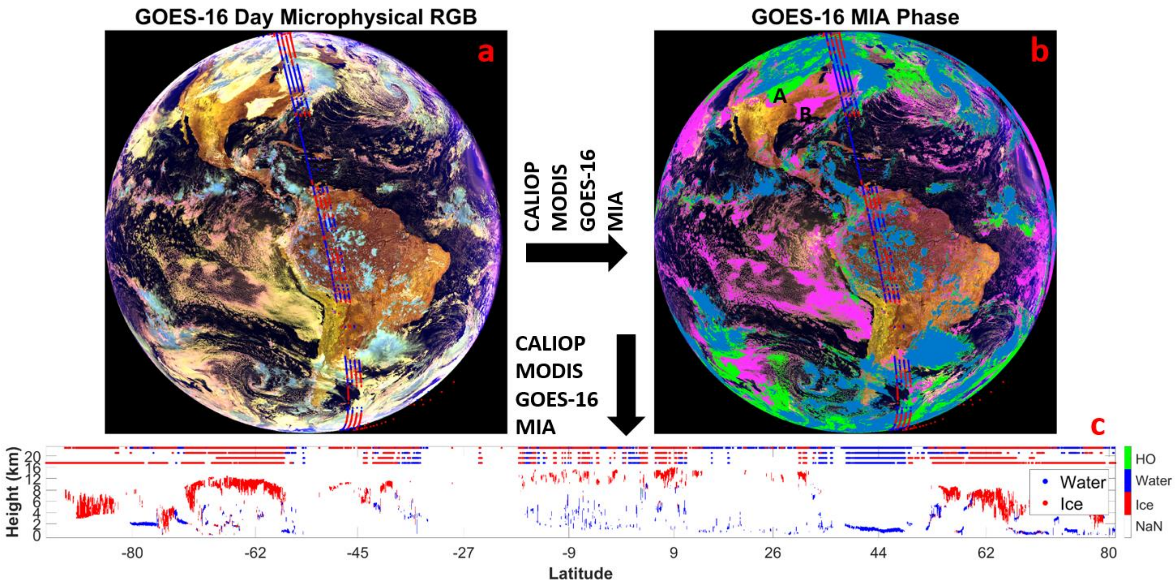

Figure 4. (a) DMRGB overlapped with CTP_CALIOP, CTP_MODIS, CTP_GOES, and CTP_MIA (dotted lines from left to right). Red dots are ice phase pixels and blue dots are liquid phase pixels. (b) CTP_MIA mask overlapped with identical dotted lines as in (a). In (b), pink shading is liquid phase, green shading is supercool liquid phase, and blue shading is ice phase. (c) CALIOP vertical phase mask overlapped with identical dotted lines as in (a) and (b), where DMRGB is the top line.

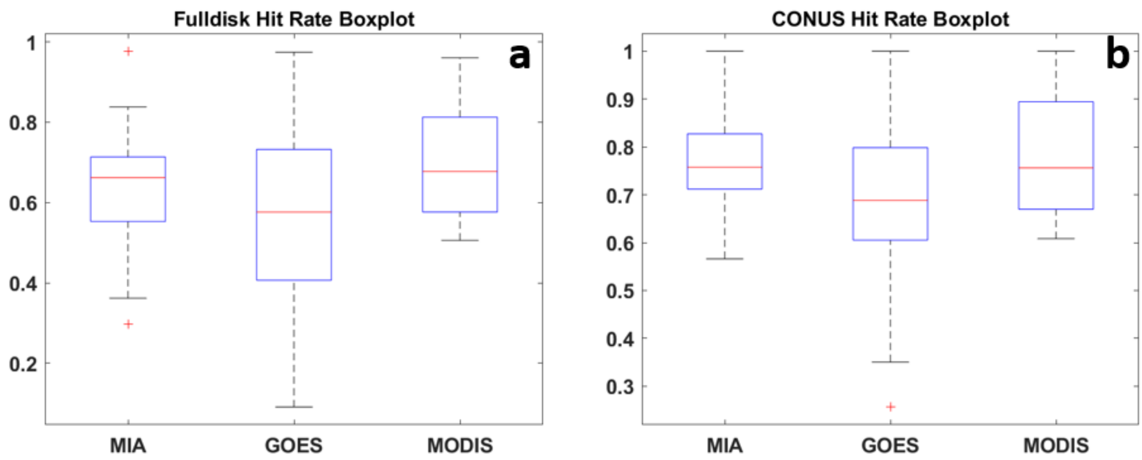

Figure 5. Boxplots of HIT_MIA, HIT_GOES, and HIT_MODIS for both FD (a) and CONUS (b) domains.

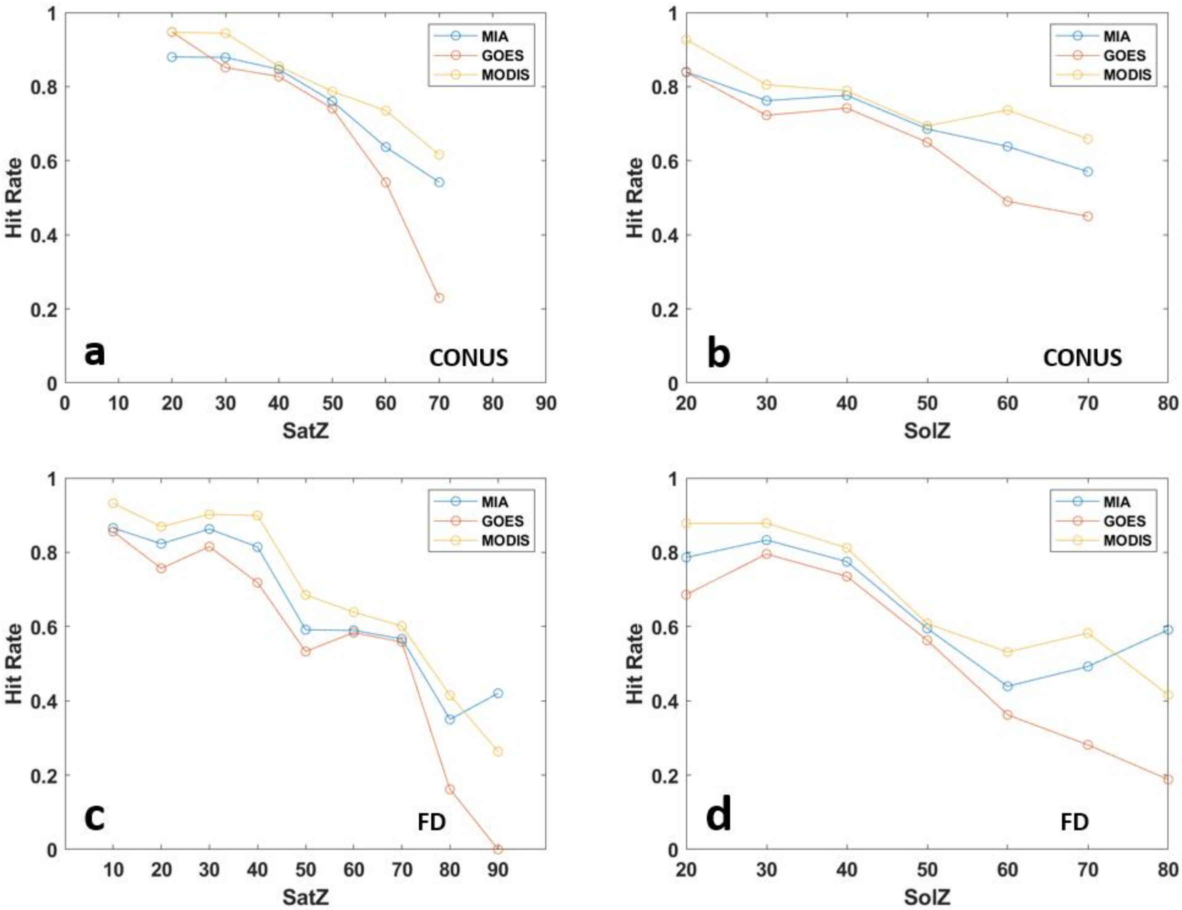

Figure 6. Median hit rate distributions for CTP_MIA, CTP_GOES, and CTP_MODIS with respect to the range of solar and satellite zenith angle covered by

CONUS and FD data.

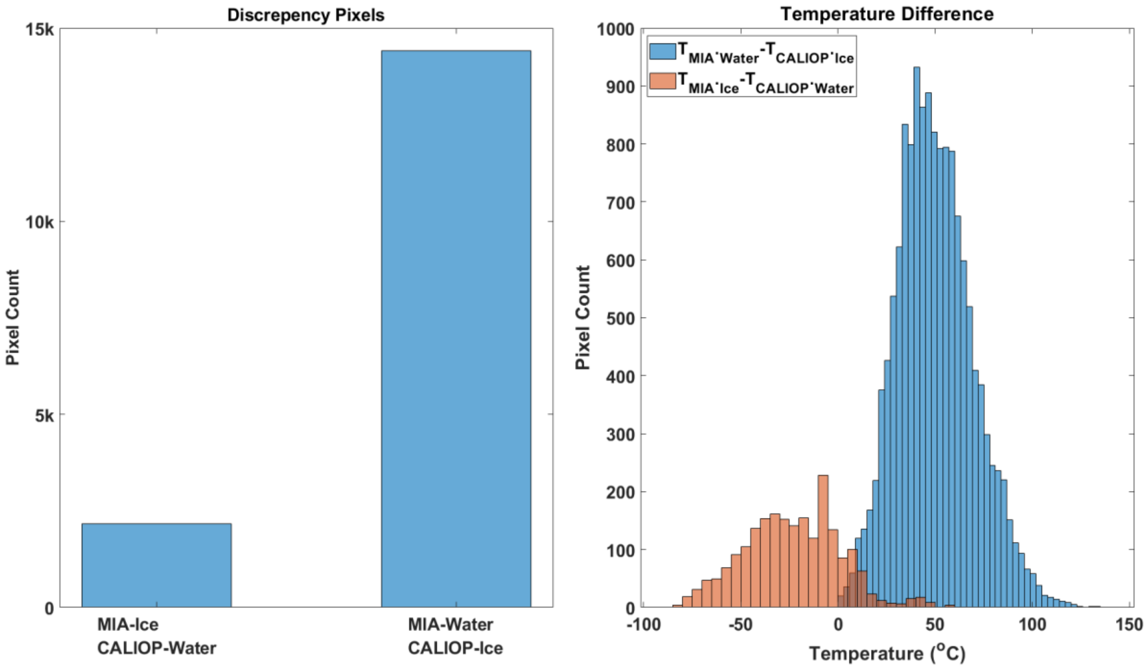

Figure 7. (a) Histogram of CTP_MIA phase pixels that are different from CTP_CALIOP. (b) The cloud-top temperature difference distribution for cases when (blue) CTP_MIA has water and CTP_CALIOP has ice and when (orange) CTP_MIA has ice and CTP_CALIOP has water.

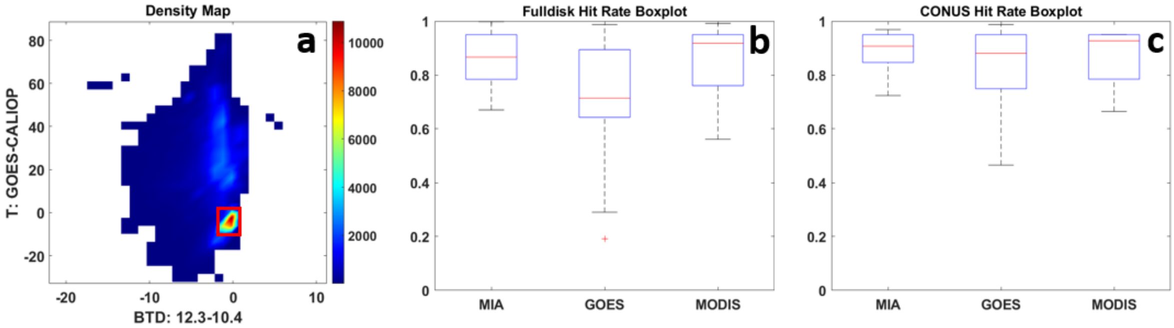

Figure 8. (a) Density map of temperature difference between GOES-16 and CALIPSO versus brightness temperature difference between 12.3 µm and 10.4 µm. (b) Boxplots as in Figure 5 after the multi-layer cloud correction for FD and (c) CONUS.